



## Fully magnetic manganite spin filter tunnel junctions

Bhagwati Prasad<sup>a)</sup> and Mark G. Blamire<sup>a)</sup>

Department of Materials Science and Metallurgy, University of Cambridge, 27 Charles Babbage Road, Cambridge CB3 0FS, United Kingdom

(Received 10 August 2016; accepted 19 September 2016; published online 29 September 2016)

In this paper we demonstrate spintronic devices which combine magnetic tunnel junctions with a spin-filtering tunnel barrier. These consist of an ultrathin ferromagnetic insulating barrier,  $\text{Sm}_{0.75}\text{Sr}_{0.25}\text{MnO}_3$ , sandwiched between two ferromagnetic half-metallic manganite electrodes,  $\text{La}_{0.7}\text{Sr}_{0.3}\text{MnO}_3$  and  $\text{La}_{0.7}\text{Ca}_{0.3}\text{MnO}_3$ , in a nanopillar structure. Depending on the relative magnetic configurations of barrier and electrode layers, three resistance states are well defined, which therefore represent a potential three-state memory concept. These results open the way for the development of spintronic devices by exploiting the many degrees of freedom of perovskite manganite heterostructure systems. *Published by AIP Publishing.* [<http://dx.doi.org/10.1063/1.4963845>]

Over the last two decades, magnetic tunnel junctions (MTJs) and spin filter tunnel junctions (SFTJs) have been explored extensively for the generation of highly spin polarized tunneling currents.<sup>1–7</sup> By exploiting the dependency of the degree of spin polarization of tunneling current on the spin density of states (DOSs) of ferromagnetic electrodes in MTJs and the spin-dependent dependent barrier heights in SFTJs at the same time, one can potentially generate very high spin-polarized tunnel current through a ferromagnetic metal (FM)/ferromagnetic insulator (FMI)/ferromagnetic metal tunnel junction. The concept of such fully magnetic tunnel junction has theoretically been proposed recently;<sup>8–10</sup> however, the experimental verification of this model has not been demonstrated yet. Sánchez *et al.*<sup>11</sup> have recently suggested the realization of all-oxide magnetic tunnel junctions with epitaxial  $\text{SrRuO}_3/\text{CoFe}_2\text{O}_4/\text{La}_{2/3}\text{Sr}_{1/3}\text{MnO}_3$  trilayer structure. Ferromagnetic metallic manganites are half-metallic and therefore can be explored as electrodes with a ferromagnetic insulating manganite tunnel barrier in fully magnetic tunnel junctions. Moreover, the crystallographic compatibility barrier layer and electrodes (perovskite structure with small lattice mismatch) are expected to give rise to perfect epitaxial interfaces.

The epitaxial growth and ferromagnetic insulating behavior of  $\text{Sm}_{0.75}\text{Sr}_{0.25}\text{MnO}_3$  (SSMO) thin films have been demonstrated in our earlier studies.<sup>12</sup> Half-metallic ferromagnetic manganites,  $\text{La}_{0.7}\text{Ca}_{0.3}\text{MnO}_3$  (LCMO) and  $\text{La}_{0.7}\text{Sr}_{0.3}\text{MnO}_3$  (LSMO), have already been well explored as electrodes in MTJs.<sup>13,14</sup> In this letter, we demonstrate the realization of epitaxially grown LCMO/SSMO/LSMO heterostructure-based fully magnetic manganite tunnel junctions as a combination of MTJs and SFTJs.

Epitaxial SSMO, LCMO, LSMO single layer, and the LCMO/SSMO/LSMO trilayer films were grown on  $\text{SrTiO}_3$  (STO) (001) single-crystalline substrates by pulsed laser deposition using a KrF laser ( $\lambda = 248$  nm). Stoichiometric ceramic targets, prepared by a standard solid-state reaction method, were ablated to grow these films at a repetition rate of 5 Hz and a fluence of  $\sim 1$  J/cm<sup>2</sup>. Nitrous oxide ( $\text{N}_2\text{O}$ ) gas

with the partial pressure of 20 Pa was used to maintain the oxygen stoichiometry during the growth of the film at a substrate temperature of 700 °C. Further, the grown films were cooled down to room temperature in 100 Pa  $\text{N}_2\text{O}$ , by switching off the heater. The growth of the LCMO/SSMO/LSMO trilayer film was investigated by high-resolution transmission electron microscopy (HRTEM). Cross-sectional specimens for HRTEM characterizations were prepared by mechanical tripod polishing followed by short ion-milling at low ion kinetic energy ( $< 1$  keV) and liquid nitrogen temperature. The material was analyzed in a JEOL ARM200CF operated at 200 keV. Weighted principal component analysis (Plugin in Gatan Digital Micrograph software, M. Watanabe, HREM Research) was performed to reduce the noise of the high-angle annular dark-field (HAADF) images and electron energy loss spectroscopy (EELS) spectrum images. Fig. 1(a) shows the cross-sectional HAADF image of a LCMO/SSMO ( $\approx 30$  nm)/LSMO film. In this imaging mode the image intensity scales with  $Z^{1.7}$ , where  $Z$  is the atomic number. Therefore, the SSMO layer appears brighter than the surrounding LSMO and LCMO layers. Note the waviness of the interfaces with amplitude of several atomic layers, and thereby the interfaces do not seem very well defined. This is also visible in the chemical distribution across the interface (Fig. 1(b)) examined by EELS. The EELS spectrum image

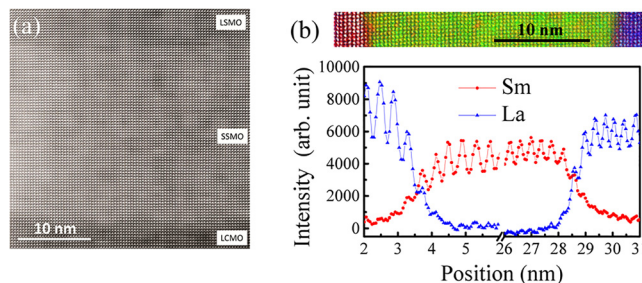


FIG. 1. (a) Cross-sectional HAADF image of a LCMO/SSMO/LSMO film grown on STO(001). The SSMO layer appears bright because of the high average atomic number of its constituents. (b) Distribution of A-site atoms in the multilayer. Top: EELS spectrum image of the layer system (left: LSMO, center: SSMO, and right: LCMO). Bottom: EELS intensity integrated along the horizontal axis of the EELS spectrum image. La and Sm intensities vary gradually across the interfaces, i.e., the interfaces are not atomically sharp.

<sup>a)</sup> Authors to whom correspondence should be addressed. Electronic addresses: bprasaditk@gmail.com and mb52@cam.ac.uk

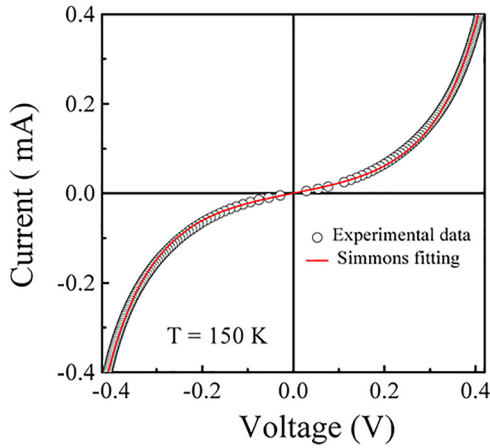


FIG. 2. The  $I$ - $V$  curve (black circles) of a LCMO/SSMO (8 nm)/LSMO tunnel junction measured at 150 K along with the Simmons fitting (red line).

and the corresponding elemental line profiles exhibit an interface chemistry that is not atomically abrupt. Such intermixing of ions at the interfaces is well observed in perovskite oxide heterostructure systems.<sup>15–17</sup>

Before the fabrication of the device, a polycrystalline gold film (thickness  $\sim 200$  nm) as a top contact layer was deposited by DC magnetron sputtering on the trilayer oxide thin films, which also serves as a protecting layer for

minimizing the ion-beam damage from the subsequent fabrication processes. First, conventional optical photolithography and argon ion milling were used to create a series of  $4\ \mu\text{m}$  wide tracks. Subsequently, nanopillar devices of an average dimension of  $500 \times 500\ \text{nm}^2$  were fabricated by focused ion beam (FIB) nanomachining.<sup>18</sup> The magnetic measurements of the unpatterned films were carried out in a vibrating sample magnetometer where the magnetic field was applied in plane. For the transport measurement of the unpatterned films and devices, the electrical contacts were made by wire bonding. The electrical measurements of the sample were performed in four-point current biased configuration in a closed-cycle He cryostat system.

The non-linear shape of the  $I$ - $V$  curve (Fig. 2) of a LCMO/SSMO (8 nm)/LSMO tunnel junction measured at 150 K reveals that tunneling is the dominant mode of electron transport across the junction. The mean barrier height of the junction is estimated to be  $\sim 0.5$  eV by fitting the experimental  $I$ - $V$  curve to the Simmons model.<sup>19</sup> In order to investigate the role of each magnetic layer in LCMO/SSMO/LSMO tunnel junctions, the magnetic field dependence of the junction resistances were measured. The distinct magnetic switching of these layers is first confirmed by the  $M$ - $H$  measurements. The hysteresis loop of a 200 nm thick SSMO film at 5 K (Fig. 3(a)) shows that the magnetization of the

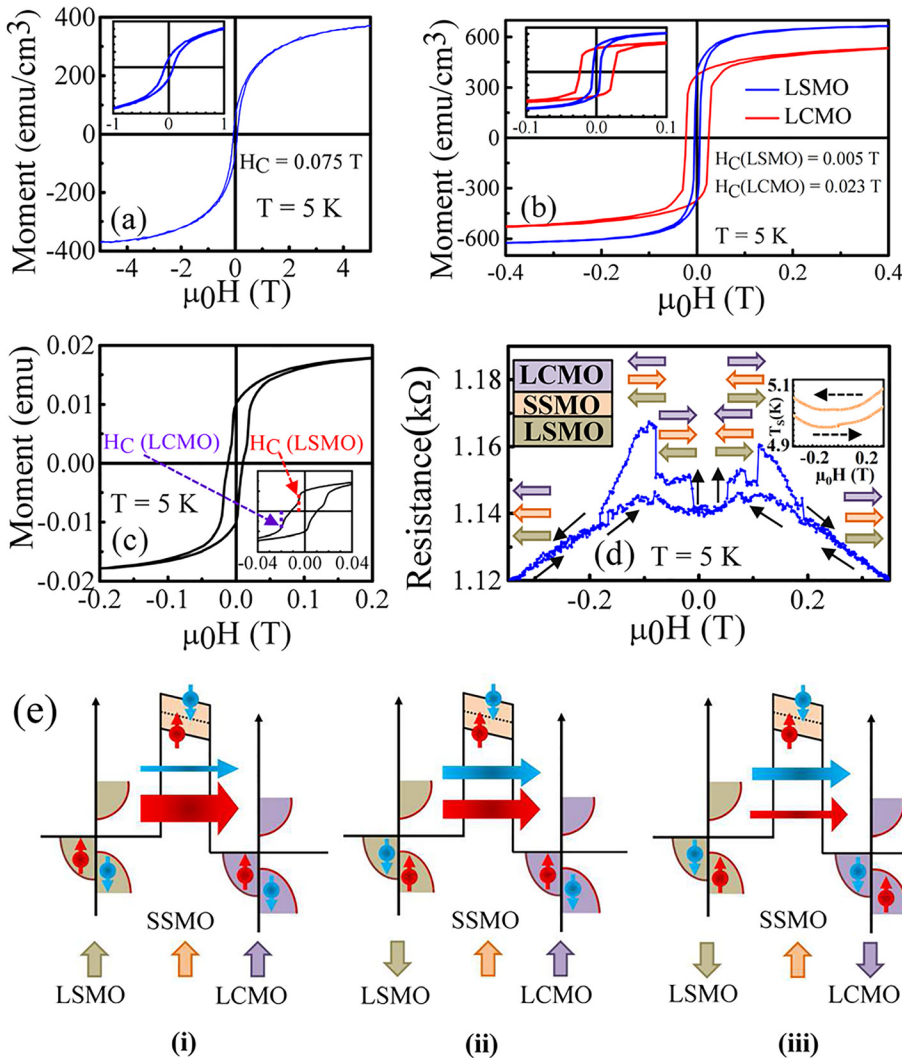


FIG. 3. The  $M$ - $H$  loops of a 200 nm thick (a) SSMO, and (b) LSMO and LCMO films measured at 5 K. Insets show a close up of the  $M$ - $H$  loop around 0 T. (c) The  $M$ - $H$  curve of a LCMO/SSMO (8 nm)/LSMO trilayer film, grown on STO (001) substrate, measured at 5 K. Inset depicts an enlarged view of the  $M$ - $H$  loop around 0 T. The arrows indicate the magnetic reversals of LCMO and LSMO films. (d) The magnetic field dependence of the junction resistance of a LCMO/SSMO/LSMO device, measured at 5 K. The thick arrows are corresponding to the magnetic orientations of barrier and electrode layers. The inset shows the variation in the sample temperature during the cycle of magnetic field, which indicates the insignificant role of thermal fluctuations. (e) Schematic illustration of a fully magnetic tunnel junction. Depending on the magnetic configurations of barrier and electrode layers, the junction exhibits (i) low ( $R_{\uparrow\uparrow\uparrow}$ ), (ii) high ( $R_{\uparrow\uparrow\downarrow}$ ), and (iii) the highest ( $R_{\downarrow\uparrow\downarrow}$ ) resistance states, respectively.

film is not saturated even at a very high magnetic field (5 T). This is probably due to the presence of antiferromagnetic phase along with ferromagnetic phase of SSMO.<sup>20</sup> The coercivity of the film is found to be  $\sim 0.075$  T. The nearly vertical and rectangular shape of the hysteresis loops of 200 nm films of LCMO and LSMO (Fig. 3(b)) at 5 K suggests the ideal ferromagnetic characteristic of these films with the coercivities of 0.023 T and 0.005 T, respectively. Such coercivity contrast observed in these films is appropriate for realizing the tunnel magnetoresistance (TMR) response in LCMO/SSMO/LSMO magnetic tunnel junctions.

Fig. 3(c) shows the magnetic hysteresis curve of a LCMO/SSMO ( $\sim 8$  nm)/LSMO trilayer film. We can see independent switching of LSMO and LCMO layers, but they are not abrupt; since the ferromagnetic properties of these layers are retained near the interface, these layers do not magnetically decouple completely. Fig. 3(d) shows the magnetic field dependent junction resistance of a LCMO/SSMO/LSMO tunnel junction at 5 K measured with an applied current bias of 0.45 mA. The tunneling conductance and the TMR of a FM/FMI/FM tunnel junction depends on magnetic configurations of ferromagnetic electrodes as well as of the ferromagnetic barrier layers.<sup>8</sup> Depending on the magnetic configuration of electrode and barrier layers, the device can attain three different resistance states:  $R_{\uparrow\uparrow\uparrow}$  (see Fig. 3(e-i)), when all three magnetic layers are in parallel configuration;  $R_{\downarrow\uparrow\uparrow}$  (see Fig. 3(e-ii)), when the LCMO and LSMO layers are antiparallel; and  $R_{\downarrow\uparrow\downarrow}$  (see Fig. 3(e-iii)), when the magnetic configuration of SSMO layer is antiparallel to both the LSMO and LCMO layers. Although the variation in sample temperature during the measurement was insignificant (see inset of Fig. 3(d)), the disparity between the  $R$ - $H$  and  $T$ - $H$  plots clearly discards the role of any thermal fluctuation in the observed switchings. These results are in consistence with the theoretical models.<sup>8,10</sup> The switching fields corresponding to the magnetic layers here are larger than the corresponding coercivities observed in  $M$ - $H$  measurements; however, such a discrepancy is consistent with the data obtained from other nanopillar tunnel devices reported earlier,<sup>21</sup> and is probably due to their smaller dimensions and the defects introduced in these layers during the fabrication process.<sup>22</sup> The sharp switchings at lower fields correspond to the magnetic reversal of LSMO and LCMO layers; however, the smooth transition at higher fields back to the background is attributed to the small remanence of the SSMO layer; thus, the fraction of SSMO aligned with the field is continuously changing. Here the TMR ratio of the device is defined as  $(R - R_{PP})/R_{PP}$ , where  $R$  is the tunnel resistance of the device when one of the magnetic layers is antiparallel to others and  $R_{PP}$  is when all three layers are parallel (at  $\mu_0 H = 0.25$  T) to each other. The TMR ratios corresponding to the high ( $R_{\downarrow\uparrow\uparrow}$ ) and the highest ( $R_{\downarrow\uparrow\downarrow}$ ) resistance states are  $\sim 1.7\%$  and  $\sim 3.3\%$ , respectively. Such low values of the TMR in our devices are possibly due to the low spin polarizations of LSMO and LCMO electrodes at the SSMO interface, which can be explained by the following model.

This model assumes zero bias and therefore the tunneling conductance via Fermi's golden rule is simply proportional to the product of the (spin-dependent) tunneling DOSs ( $D$ ) in both electrodes at Fermi level and the (spin-dependent)

barrier transmission ( $T$ ). Assuming identical electrodes, the conventional TMR ( $\eta_{\uparrow\downarrow}$ ) of a FM/FMI/FM tunnel junction is given by

$$\eta_{\uparrow\downarrow} = \eta_{\downarrow\uparrow} = \frac{R_{\uparrow\uparrow\downarrow} - R_{\uparrow\uparrow\uparrow}}{R_{\uparrow\uparrow\uparrow}} = \frac{\sigma_{\uparrow\uparrow\downarrow}}{\sigma_{\uparrow\uparrow\uparrow}} - 1 = \frac{D_{\uparrow}T_{\uparrow}D_{\uparrow} + D_{\downarrow}T_{\downarrow}D_{\downarrow}}{D_{\uparrow}T_{\uparrow}D_{\downarrow} + D_{\downarrow}T_{\downarrow}D_{\uparrow}} - 1. \quad (1)$$

Here,  $R_{\uparrow\uparrow\uparrow}(\sigma_{\uparrow\uparrow\uparrow})$  and  $R_{\uparrow\uparrow\downarrow}(\sigma_{\uparrow\uparrow\downarrow})$  are the resistances (conductivities) of the device when the ferromagnetic electrodes are parallel and antiparallel configurations, respectively. However, the magnetic configuration of the FMI barrier is parallel to one of the electrodes in both parallel and antiparallel configurations of the electrode layers.

For a conventional FM/I/FM junction this (Eq. (1)) simplifies to

$$\eta_{\uparrow\downarrow} = \frac{D_{\uparrow}D_{\uparrow} + D_{\downarrow}D_{\downarrow}}{2D_{\uparrow}D_{\downarrow}} - 1 = \frac{\left(\frac{1+P}{1-P}\right)^2 + 1}{2\left(\frac{1+P}{1-P}\right)} - 1 = \frac{2P^2}{(1+P)(1-P)},$$

where the spin polarization ( $P$ ) of electrode layer is given by

$$P = \frac{D_{\uparrow} - D_{\downarrow}}{D_{\uparrow} + D_{\downarrow}}.$$

The conventional TMR (Eq. (1)) of a FM/FMI/FM tunnel junction in terms of electrode spin polarization ( $P$ ) can be expressed as

$$\eta_{\uparrow\downarrow} = \frac{\left(\frac{1+P}{1-P}\right)^2 T_{\uparrow} + T_{\downarrow}}{\left(\frac{1+P}{1-P}\right)(T_{\uparrow} + T_{\downarrow})} - 1 = \frac{(1+P)^2 T_{\uparrow} + (1-P)^2 T_{\downarrow} - (1-P^2)(T_{\uparrow} + T_{\downarrow})}{(1-P^2)(T_{\uparrow} + T_{\downarrow})} = \frac{2P(T_{\uparrow} - T_{\downarrow}) + 2P^2(T_{\uparrow} + T_{\downarrow})}{(1-P^2)(T_{\uparrow} + T_{\downarrow})}.$$

For a conventional FM/I/FM junction (i.e.,  $T_{\uparrow} = T_{\downarrow}$ ), the TMR is defined as

$$\eta_{\uparrow\downarrow} = \frac{2P^2}{(1-P^2)}. \quad (2)$$

However, in the high spin filter limit (i.e.,  $T_{\uparrow} \gg T_{\downarrow}$ ), the TMR for a FM/FMI/FM tunnel junction can be simplified as

$$\eta_{\uparrow\downarrow} = \frac{2P(1+P)}{(1-P^2)} = \frac{2P}{(1-P)}. \quad (3)$$

By symmetry

$$\eta_{\uparrow\uparrow\downarrow} = \eta_{\downarrow\uparrow\uparrow} = \eta_{\uparrow\downarrow\downarrow} = \eta_{\downarrow\downarrow\uparrow}.$$

On the other hand, the spin filter MR is given by

$$\begin{aligned} \eta_{\uparrow\downarrow\uparrow} &= \frac{R_{\uparrow\downarrow\uparrow} - R_{\uparrow\uparrow\uparrow}}{R_{\uparrow\uparrow\uparrow}} = \frac{\sigma_{\uparrow\uparrow\uparrow}}{\sigma_{\uparrow\downarrow\uparrow}} - 1 = \frac{D_{\uparrow}T_{\uparrow}D_{\uparrow} + D_{\downarrow}T_{\downarrow}D_{\downarrow}}{D_{\uparrow}T_{\downarrow}D_{\uparrow} + D_{\downarrow}T_{\uparrow}D_{\downarrow}} - 1, \\ \eta_{\uparrow\downarrow\uparrow} &= \eta_{\downarrow\uparrow\downarrow} = \frac{\left(\frac{1+P}{1-P}\right)^2 T_{\uparrow} + T_{\downarrow}}{\left(\frac{1+P}{1-P}\right)^2 T_{\downarrow} + T_{\uparrow}} - 1 \\ &= \frac{\left(\frac{1+P}{1-P}\right)^2 (T_{\uparrow} - T_{\downarrow}) + (T_{\downarrow} - T_{\uparrow})}{\left(\frac{1+P}{1-P}\right)^2 T_{\downarrow} + T_{\uparrow}} \\ &= \frac{4P(T_{\uparrow} - T_{\downarrow})}{(1+P)^2 T_{\downarrow} + T_{\uparrow}(1-P)^2}. \end{aligned}$$

As expected, this becomes zero for a non-spin filtering barrier (i.e.,  $T_{\uparrow} = T_{\downarrow}$ ).

However, in the high spin filter limit (i.e.,  $T_{\uparrow} \gg T_{\downarrow}$ ) for values of  $P$  which are not too large, the spin filter MR can be simplified as

$$\eta_{\uparrow\downarrow\uparrow} \simeq \frac{4P}{(1-P)^2}. \quad (4)$$

The ratio of spin-filter MR/TMR for a FM/FMI/FM tunnel junction for low values of  $P$  is therefore approximately given by

$$\eta_{\uparrow\downarrow\uparrow} \simeq \frac{4P}{(1-P)^2} \frac{(1-P)}{2P} \simeq \frac{2}{(1-P)} \simeq 2,$$

i.e., the TMR% for the antiparallel configuration of electrodes should be twice the TMR% for parallel configuration in the limit of low electrode/interface polarization and high barrier polarization. This suggests that the TMR values are independent of the spin filtering and just dependent on the electrode/interface spin polarization. The TMR ratio corresponding to the highest resistance state in our device is twice that of the high resistance state, which is in agreement with the proposed model. This is corroborated by the fact that the interfaces between SSMO and LSMO/LCMO are not very well defined (Fig. 1) and therefore that spin-disorder clusters present at the interfaces modify the interfacial density of states and thereby reduce the LSMO/LCMO spin polarization at the SSMO interface.<sup>23,24</sup> Intercalating an ultrathin STO layer between LSMO/LCMO and SSMO layers could prevent the formation of spin-disorder clusters at the interfaces and also decouple the magnetic interaction of these layers;<sup>25</sup> however, fabrication and measurement of such devices is very challenging due to the involvement of three barrier layers. Moreover, the absence of sharp magnetic switching in the SSMO layer inhibits the device from attaining the perfect antiparallel magnetization state and hence low TMR.

Although the TMR of LCMO/SSMO/LSMO tunnel device is quite low, the three well-defined distinct resistance states in the  $R$  vs  $H$  plot confirm the spin dependent tunneling of the electrons through the FMI (SSMO) tunnel barrier with

ferromagnetic electrodes. We have observed such behavior in several other tunnel junctions and therefore our manganite-based fully magnetic tunnel junctions define a three resistance state systems. Gajek *et al.*<sup>3</sup> have observed four resistance states in multiferroic,  $\text{La}_{0.1}\text{Bi}_{0.9}\text{MnO}_3$ -based spin filter tunnel junctions. Introducing such multiferroic barrier in fully magnetic tunnel junctions with appropriate magnetic decoupling layers can provide an opportunity to explore several functionalities of the tunnel barriers.

To conclude, the potential of manganite-based full magnetic tunnel junctions to generate the highly spin polarized current has been realized. Our devices showed the highest resistance state when magnetic configuration of electrode layers are parallel to each other but antiparallel to that of the barrier layer, whereas the low resistance state appeared when both electrodes and barrier layer are parallel. However, in the case of antiparallel magnetic configuration of the electrode layers, the devices showed the intermediate (high) resistance state. Such three distinct resistance states can be used to encode ternary information. The tunnel magnetoresistance ratios corresponding to higher and highest resistance states are  $\sim 1.7\%$  and  $\sim 3.3\%$ , respectively, that can be enhanced significantly by decoupling these magnetic layers. These results open an avenue for exploring electric field-controlled ternary state spintronic devices.

This work was partially supported by the ERC Advanced Integrators Grant ‘‘SUPERSPIN’’. B.P. was funded by the Nehru Trust for Cambridge University and St. John’s College. We thank Ute Salzberger and Wilfried Sigle (Max Planck Institute for Solid State Research, Stuttgart, Germany) for careful TEM specimen preparation and characterization, respectively.

- <sup>1</sup>J. S. Moodera, L. R. Kinder, T. M. Wong, and R. Meservey, *Phys. Rev. Lett.* **74**, 3273 (1995).
- <sup>2</sup>E. Y. Tsymal, O. N. Mryasov, and P. R. LeClair, *J. Phys.: Condens. Matter* **15**, R109 (2003).
- <sup>3</sup>M. Gajek, M. Bibes, S. Fusil, K. Bouzouane, J. Fontcuberta, A. Barthélemy, and A. Fert, *Nat. Mater.* **6**, 296 (2007).
- <sup>4</sup>C. Chappert, A. Fert, and F. N. Van Dau, *Nat. Mater.* **6**, 813 (2007).
- <sup>5</sup>T. Nagahama, T. Santos, and J. Moodera, *Phys. Rev. Lett.* **99**, 016602 (2007).
- <sup>6</sup>J. S. Moodera, T. S. Santos, and T. Nagahama, *J. Phys.: Condens. Matter* **19**, 165202 (2007).
- <sup>7</sup>G.-X. Miao, J. Chang, B. A. Assaf, D. Heiman, and J. S. Moodera, *Nat. Commun.* **5**, 3682 (2014).
- <sup>8</sup>Y. Li, B.-Z. Li, W.-S. Zhang, and D.-S. Dai, *Phys. Rev. B* **57**, 1079 (1998).
- <sup>9</sup>D. Jin, Y. Ren, Z. Li, M. Xiao, G. Jin, and A. Hu, *J. Appl. Phys.* **99**, 08T304 (2006).
- <sup>10</sup>D. Jin, Y. Ren, Z. Li, M. Xiao, G. Jin, and A. Hu, *Phys. Rev. B* **73**, 012144 (2006).
- <sup>11</sup>A. M. Sánchez, L. Äkäslompolo, Q. H. Qin, and S. van Dijken, *Cryst. Growth Des.* **12**, 954 (2012).
- <sup>12</sup>B. Prasad, M. Egilmez, F. Schoofs, T. Fix, M. E. Vickers, W. Zhang, J. Jian, H. Wang, and M. G. Blamire, *Nano Lett.* **14**, 2789 (2014).
- <sup>13</sup>N. V. Volkov, *Phys. - Usp.* **55**, 250 (2012).
- <sup>14</sup>M. Bowen, M. Bibes, A. Barthélemy, J.-P. Contour, A. Anane, Y. Lemaître, and A. Fert, *Appl. Phys. Lett.* **82**, 233 (2003).
- <sup>15</sup>Y.-M. Kim, A. Morozovska, E. Eliseev, M. P. Oxley, R. Mishra, S. M. Selbach, T. Grande, S. T. Pantelides, S. V. Kalinin, and A. Y. Borisevich, *Nat. Mater.* **13**, 1019 (2014).
- <sup>16</sup>L. Feng, S. Yang, Y. Lin, D. Zhang, W. Huang, W. Zhao, Y. Yin, S. Dong, and X. Li, *ACS Appl. Mater. Interfaces* **7**, 26036 (2015).
- <sup>17</sup>M. Gibert, M. Viret, A. Torres-Pardo, C. Piamonteze, P. Zubko, N. Jaouen, J. M. Tonnerre, A. Mougín, J. Fowlie, S. Catalano, A. Gloter, O. Stéphan, and J. M. Triscone, *Nano Lett.* **15**, 7355 (2015).
- <sup>18</sup>C. Bell, G. Burnell, D.-J. Kang, R. H. Hadfield, M. J. Kappers, and M. G. Blamire, *Nanotechnology* **14**, 630 (2003).

<sup>19</sup>J. G. Simmons, *J. Appl. Phys.* **34**, 1793 (1963).

<sup>20</sup>A. I. Kurbakov, *J. Magn. Magn. Mater.* **322**, 967 (2010).

<sup>21</sup>B. Prasad, W. Zhang, J. Jian, H. Wang, and M. G. Blamire, *Adv. Mater.* **27**, 3079 (2015).

<sup>22</sup>A. G. Kolhatkar, A. C. Jamison, D. Litvinov, R. C. Willson, and T. R. Lee, *Int. J. Mol. Sci.* **14**, 15977 (2013).

<sup>23</sup>F. Mezei and A. Zawadowski, *Phys. Rev. B* **3**, 3127 (1971).

<sup>24</sup>P. LeClair, J. T. Kohlhepp, H. J. M. Swagten, and W. J. M. de Jonge, *Phys. Rev. Lett.* **86**, 1066 (2001).

<sup>25</sup>T. Harada, I. Ohkubo, M. Lippmaa, Y. Sakurai, Y. Matsumoto, S. Muto, H. Koinuma, and M. Oshima, *Adv. Funct. Mater.* **22**, 4471 (2012).